Deep Resources Engineering 3 (2026) 100208

Contents lists available at ScienceDirect

Deep Resources Engineering

journal homepage: www.keaipublishing.com/en/journals/deepre/

Full length article

Numerical study on the mechanism of tool impact fragmentation in heterogeneous rock under confining pressure

Huihe Zhao [a], Hongxiang Jiang [a,b,*], Zijian Wu [a], Dongsheng Zhao [a], Airong Wang [a]

[a] College of Mechanical and Electrical Engineering, China University of Mining and Technology, Xuzhou 221116, China
[b] Jiangsu Collaborative Innovation Center of Intelligent Mining Equipment, China University of Mining and Technology, Xuzhou 221008, China

ARTICLE INFO

Keywords:
Mechanical impact
Heterogeneous rock
Confining pressure
Rock-breaking mechanism

ABSTRACT

To address the problems of damage observation and stress extraction during the impact breaking of granite by tools under confining pressure, a numerical model for the fragmentation of heterogeneous rocks by hammer-tool impact was established based on the pre-processing model modifications. The crack propagation and damage distribution of heterogeneous rock impacted by machinery were studied in this article. The results indicate that during tool impact rock breaking, the rock at the impact point mainly experiences compression and shear failure, whereas tensile stress dominates the propagation of rock cracks around the point of impact. Interlayer distribution and boundary layer ambiguity exist in the propagation of stress waves in heterogeneous rocks. The confining pressure primarily suppresses the propagation of internal cracks and damage in rocks, as it influences tensile and shear stresses. The research results provide a theoretical reference for improving the efficiency of rock breaking by mining machinery impact.

1. Introduction

The equipment of mechanical rock breaking is widely used in fields such as fossil energy extraction, tunnel excavation, and municipal engineering [1–3]. The rock breaking methods (Impact, Cutting, Indentation) of different mechanical equipment are different, resulting in differences in the size of rock debris. The size of rock debris is one of the important indicators for measuring the specific energy consumption of rock breaking. The smaller the size of rock debris, the higher the specific energy consumption, and vice versa. As shown in Fig. 1, the size of rock debris from different rock break equipment indirectly reflects that impact rock breaking has a relatively high rock breaking efficiency, low energy consumption, and tool consumption [4–7]. However, in the process of extracting deep strategic mineral resources, the mechanism of mechanical fragmentation of hard rocks is still unclear due to the anisotropy, heterogeneity, and no transparency of natural rocks, high surrounding rock stress, and other environmental conditions [8–10]. How to achieve efficient crushing of extremely hard and high-wear-resistant rocks under confining pressure has become a key issue in the rapid excavation of deep hard rocks. To improve the efficiency of impact rock breaking, researchers in this field have conducted extensive research on the theoretical model, performance, and mechanism of impact rock breaking through experimental and numerical simulation methods.

Cao et al. [11] used various resonance detection methods to reconstruct the microstructure inside the rock after impact loading and studied the distributions of damage, crack propagation, and pore changes inside the rock. Natural rock formations at significant depths are characterized by inherent joint structures and are subjected to substantial in-situ stress conditions, both of which significantly influence the efficiency of rock fragmentation processes. To study this issue, Zhang et al. [12] analyzed the effect of confining pressure on the damage distribution of mechanically impact-fractured granite using infrared nondestructive testing technology. Li et al. [13] studied the macroscopic characteristics and crack propagation laws of mechanical impact rock breaking under confining pressure and static water column pressure through single-ball tooth impact rock breaking experiments. Wang et al. [14] also studied the effects of confining pressure and joint factors on rock stress evolution and fracture behavior under mechanical impact. However, the rock fragmentation process under impact loading occurs within an extremely short duration, making it challenging to investigate the underlying mechanisms (Fracture law) and factors influencing rock

Peer review under responsibility of Editorial Board of of Deep Resources Engineering.
* Corresponding author at: College of Mechanical and Electrical Engineering, China University of Mining and Technology, Xuzhou 221116, China.
E-mail address: jianghongxiang@cumt.edu.cn (H. Jiang).

https://doi.org/10.1016/j.deepre.2025.100208
Received 25 April 2025; Received in revised form 1 August 2025; Accepted 16 August 2025
Available online 10 November 2025

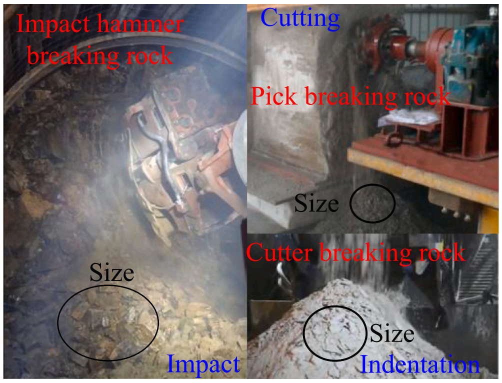

Fig. 1. Comparison of mechanical rock breaking slag size.

breakage. Wang et al. [15] used ultrahigh-speed photography technology to observe the generation and propagation process of edge cracks in granite samples under impact loads and studied the influence of impact parameters on rock fracture and fragmentation. Guo et al. [16] used high-speed cameras to monitor the fracture process of concrete under mechanical impact and studied the effects of impact parameters, concrete strength, and strain rate on the dynamic fracture behavior of concrete. Xi et al. [17] observed the generation and development of cracks during the transient fracture process of rocks using high-speed cameras and analyzed the influence of different factors on the conversion rate of mechanical impact rock-breaking fracture energy. Energy utilization efficiency is an important parameter for measuring the rock breaking performance of mechanical impact. Lu et al. [18] conducted impact rock-breaking experiments at different strain rates using a Separated Hopkinson Pressure Bar (SHPB) device to investigate the relationship between the degree of rock damage and energy dissipation rate. Wang et al. [19] systematically studied the relationship between energy dissipation rate and confining pressure of rocks under different disturbance frequencies through triaxial fatigue and multi-stage unloading confining pressure experiments. The energy dissipation characteristics exhibit a strong correlation with the propagation behavior of stress waves within rock. Hu et al. [20] used a nonmetallic acoustic velocimeter to measure the propagation speed of stress waves inside damaged and undamaged rock and analyzed the damage and fracture characteristics of rock through the variation law of damage factors. Nevertheless, it is difficult to accurately acquire stress field data and quantify internal damage distribution during high-velocity impact rock fragmentation processes. These limitations consequently hinder comprehensive investigations into rock fracture mechanisms and performance. For this reason, many scholars mostly use numerical methods to study the fragmentation mechanism of rock under impact. Jiang et al. [21] established a mechanical impact rock-breaking model based on the coupling method of finite element (FEM) method and discrete element (DEM) method and studied the rock-breaking mechanism of head impact. Tian et al. [22] further studied the stress wave propagation characteristics, energy dissipation, and damage evolution law of the rock under impact loading through numerical simulation. Numerical simulation provides an effective approach for investigating the effects of multiple factors, including impact parameters, rock-breaking methodologies, and geological conditions, on the mechanisms of rock fragmentation processes. Jiang et al. [23] studied the microscopic damage, stress, and crack distribution inside rocks under the combined impact of ball teeth and jets via the SPH-FEM method, as well as the influence of impact parameters on rock fragmentation. Li et al. [24] studied the microcrack propagation process of rocks during triaxial compression based on particle flow code (PFC) and analyzed the relationship between the number and morphology of cracks and the increment of rock damage. Jiang et al. [25] simulated the process of rock breaking by a rolling cutter via the FEM–DEM coupling method and studied the rock breaking performance and crack propagation law of advanced slotting rolling cutters. Yuan et al. [26] numerically simulated the mechanical cyclic impact rock fragmentation process under confining pressure conditions and analyzed the influence of confining pressure factors on the distribution of rock damage and crack propagation. In addition, numerical simulation can not only study mechanical rock breaking performance at multiple scales, but also has high repeatability. Zhang et al. [27] analyzed the relationship between impact rock-breaking parameters and the cutting force by establishing a DEM rock cutting numerical model under impact loading. Wang et al. [28] numerically simulated the rock-breaking process of PDC impact cutting teeth and analyzed the influence of impact parameters on their mechanical rock-breaking performance and cutting tooth temperature. Cao et al. [29] established numerical models for impact rock breaking using different tooth-shaped cutting tools based on rock mechanics and finite element theory and studied the impact rock-breaking performance of different cutting tools. Gao et al. [30] studied the effects of stress, pre-hole size, and position on the dynamic fracture characteristics of rocks by using the SHPB experiments.

According to current research, the experimental method makes accurate reproduction of the complex surrounding rock stress environment under deep-ground conditions difficult. Numerical simulation approaches frequently employ simplified representations of rocks as homogeneous media, which inevitably leads to discrepancies between the simulation results and the actual fragmentation mechanisms observed in heterogeneous rock formations. Through systematic analysis and scrutiny, it becomes evident that the conclusions derived from existing studies on impact-induced rock fragmentation remain subject to further study and exploration. This highlights the necessity for more in-depth investigations into the fracture mechanisms and crack propagation patterns in heterogeneous rock masses under complex stress conditions. Moreover, the propagation law of stress waves within heterogeneous rock, the microscopic mechanism of crack initiation and propagation, and the range of rock damage during mechanical impact rock breaking are key issues. Therefore, this work modifies the numerical model of rocks through random replacement, simulates the process of mechanical tooling impacting heterogeneous rocks, further studies the mechanism of rock fragmentation, and improves the efficiency of deep hard rock fragmentation.

2. Methods

2.1. Experimental device and numerical model

As shown in Fig. 2, the mechanical impact rock-breaking experimental device mainly includes 1) pulley, 2) lifting device, 3) impact hammer, 4) impact cylinder, 5) rock, 6) tool, with marked holes machined at intervals of 200 mm (Δh) on the impact cylinder. To study the effect of tool tooth shape on its impact rock breaking, three different tooth shapes of tools (A: Square, B: Rectangular, C: Circular) were selected for impact rock breaking experiments. The rock specimen measures 300 × 300 × 100 mm^3. The tool's handle has a diameter of 45 mm and a length of 200 mm. The impact hammer features a diameter of 156 mm and a length of 200 mm. The heads of tools are characterized as follows: Type A tool is a square with a side length of 15 mm, type B tool is a rectangular shape measuring 42.5 mm × 15 mm, and type C tool is a circular shape with a diameter of 45 mm. The impact hammers and mechanical tools in the numerical model were set up as rigid bodies with meshing dimensions based on guaranteed geometry. The mesh size of the rock can have an impact on the numerical simulation results and computational efficiency. Therefore, the C-type tool was used for trial calculations for models with different mesh sizes before performing numerical simulations. It was found that the damage and fracture effects of the rock were deviated when the mesh size of the rock was 6 mm, and the damage and fracture effects of the rock with a mesh size of 5 mm were basically the same as those with smaller mesh sizes. Considering

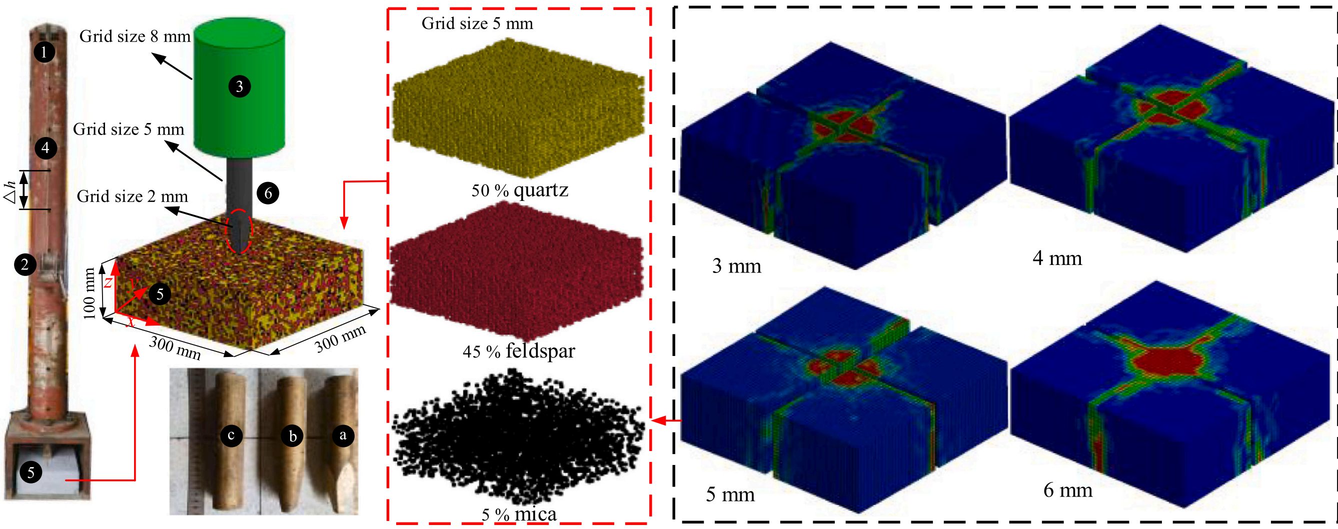

Fig. 2. Numerical modeling and mesh-independent validation of impact rock breaking by mechanical tools.

the computational efficiency of the numerical model, the 5 mm size was used for the mesh delineation of the rock model. In the numerical model, the rock grid size is 5 mm, the impact hammer grid size is 8 mm, the tool handle grid size is 5 mm, and the tool head grid size is 2 mm. The impact hammer and tool used automatic surface-to-surface contact, and the tool and rock used eroding surface-to-surface contact. According to the motion form of each component during the rock-breaking process of the cutting tool in the experiment, only the degrees of freedom of the impact hammer and the cutting tool along the impact direction are released in the numerical model. Add a Z-direction constraint to the bottom of the rock.

The homogeneous rock model was modified using MATLAB R2022b to a heterogeneous rock composed of three different minerals. As shown in Fig. 3, the modeling process of numerical models for heterogeneous rocks. The different colored rock elements in the Fig. 2 represent mineral with different attributes, and the rock elements with different attributes still maintain common node operation, which can ensure the effective transmission of stress and strain generated by tool impact inside the rock. The rock contains multiple minerals in various proportions (which may vary depending on the sampling location). The grayish-white granite used in the experiments of this literature [31] is of the same type as the rock used in this paper and has similar compressive strength. Moreover, components with relatively small proportions have little effect on the mechanical impact of rock breaking. Therefore, we determined the approximate composition ratio (50% quartz, 45% feldspar, and 5% mica) by referring to relevant literature and combining it with the rock properties used in the experiment [31].

2.2. Material model

The impact hammer and tool used in the experiment have undergone quenching treatment, with high hardness and very little deformation. Therefore, in numerical simulations, both the tool and impact hammer are modeled using rigid materials. As shown in Fig. 4, four rock elements are randomly taken from the center of the rock breaking by mechanical tool impact to the edge of the rock to analyze the change rule of its strain with time and calculate its strain rate. From the figure, the strain rate of rock breaking by drop hammer impact is basically in the range of 10 - 10^2 s^{-1} , and the strain rate is higher the closer to the impact point of the mechanical tool. The strain rate of the mechanical tool impact breaking rock studied in this paper is between low dynamic (falling hammer experiment) and high dynamic (Hopkinson bar), which belongs to the category of dynamic loading. Holmquist-Johnson-Cook, Johnson-Holmquist model, and Riedel Hiermaier Thomas are commonly used material models for studying rock fracture and fragmentation processes [32–34]. Riedel Hiermaier Thomas constitutive model is a constitutive model constructed for concrete materials, which has a good performance in characterizing the damage and crack extension of rocks under dynamic loading [35]. Therefore, this article adopts the Riedel Hiermaier Thomas constitutive model to establish a numerical model of rock.

The key to accurately reproducing the rock-breaking process of tool impact in numerical simulation lies in the rock constitutive. Therefore, this section focuses on explaining the inherent principles of numerical models and does not provide too much description of the rigid consti-

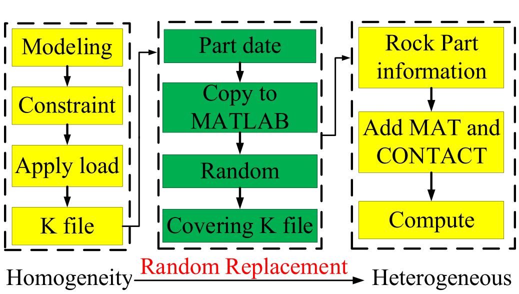

Fig. 3. Numerical modeling process for heterogeneous rocks.

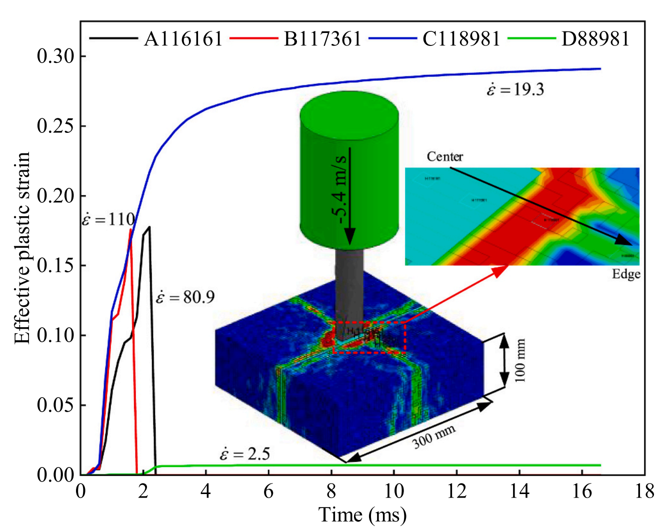

Fig. 4. Strain of rock elements at different locations.

tutive relationship of tool and impact hammer. The Riedel Hiermaier Thomas constitutive model describes the evolution of pores inside materials under external loads through the state equation of pressure porosity, and couples this equation with the strength equation to fully characterize the mechanical properties of natural rocks under pressure. As shown in Fig. 5a, when the external load (P_o) is less than the rock pore fracture pressure, small volume strain, the rock is in the stage of elastic deformation. When the external load exceeds the rock pore fragmentation pressure, the internal pores of the rock begin to rupture, and the volume strain increases with the fragmentation of the pores. At this stage, the removal of the external load on the rock generates permanent strain. When the external load continues to increase the compaction pressure, the internal pores of the rock are completely closed ($pro = 1$), and the pressure load increases exponentially, and brittle fractures may occur in the rock.

The Riedel Hiermaier Thomas model describes the strength reduction and strain rate effect of rocks along different meridians through three stress surfaces. As shown in Fig. 5b, the arrow points represent the response process of the rock during the increase of external pressure, and the left side of the vertical axis represents the rock bearing tensile load. The rock model exhibits elasticity before the stress reaches the initial yield surface. When the stress exceeds the initial yield surface, the rock will undergo plastic deformation, and an effective yield surface will be formed under the combined effect of plastic strain and model hardening characteristics. When the stress state of the rock reaches the ultimate strength on the failure surface, the damage in the model accumulates with the increase of nonlinear plastic strain, leading to the softening of the failure surface and the formation of the stress limit surface after failure, which is the residual surface. In addition, it can be seen from the graph that the change in tensile load within a small range can achieve the transformation from elastic yield surface to failure surface, which is in line with the characteristics of rock with a low tensile strength. The shear strength is only supported under restricted conditions (i.e., under normal pressure). Therefore, residual surfaces only exist in a compressed state [36].

Function expression for initial yield surface:

$$\sigma_y = f_c \sigma_y^* R_3 \tag{1}$$

where f_c is the uniaxial compressive strength; σ_y^* is a function of the failure surface function σ_f^* and plastic strain ε_p; and $R_3(\theta, P^*)$ is the deflection strength function.

$$\sigma_y^* = \sigma_f^* (\varepsilon_p^* + (1 - \varepsilon_p^*) F_e F_r) \tag{2}$$

where $\varepsilon_p^* = \varepsilon_p / f_c$ is the normalized plastic strain, F_e is the elastic strength parameter, and F_r is the yield surface limit parameter.

$$R_3 = \frac{2(1 - Q^2)\cos\theta + 2Q\sqrt{4(1 - Q^2)\cos^2\theta + 5Q^2 - 4Q}}{4(1 - Q^2)\cos^2\theta + (1 - 2Q)^2} \tag{3}$$

$$Q = Q_0 + Bp^* \tag{4}$$

where θ is the Lode angle, Q_0 and B are lord's angle coefficients.

The function expression of the failure surface function is:

$$\sigma_f^* = \begin{cases} A[p^* - F_r/3 + (A/F_r)^{-1/N}]^N & 3p^* \geq F_r \\ F_r f_s^*/Q_1 + 3p^*(1 - f_s^*/Q) & F_r > 3P^* \geq 0 \\ F_r f_s^*/Q_1 + 3P^*(1/Q_2 - f_s^*/Q_1 f_t^*) & 0 > 3p^* \geq 3p_t^* \\ 0 & 3p_t^* > 3p^* \end{cases} \tag{5}$$

where A and N are the parameters of the failure surface; f_s^*, f_t^* are the normalized shear and tensile strengths, respectively; F_r is the intensity increase factor; and p_t^* is the failure cutoff pressure.

Residual surface function expression:

$$\sigma_r^*(p^*) = A_f \{p^*\}^{n_f} \tag{6}$$

where A_f and n_f are residual surface parameters.

The extent of damage in rock elements is visually represented by color gradations, where the color intensity correlates with the density of microscopic fractures within the rock. Upon reaching complete damage, the rock element transitions to a distinctive red hue, indicating that it has attained the threshold of residual failure strength while maintaining residual compressive capacity. When such fully damaged rock elements undergo continued stress application and subsequent deformation, they activate a deletion mechanism that ultimately leads to macroscopic rock fracturing.

Expression of damage accumulation function:

$$D = \int_{\varepsilon_p^h}^{\varepsilon_p} \frac{d\varepsilon_p}{\varepsilon_p^f} \tag{7}$$

where ε_p is the plastic strain, ε_p^h is the plastic strain in the current hardened state, and ε_p^f is the plastic strain at the failure surface [37,38].

2.3. Comparison and verification

To verify the accuracy of the numerical model of rock breaking by tool impact established in this article, a series of comparative verification experiments were conducted. The rock constitutive model is verified through uniaxial compression and splitting experiments. The numerical simulation employs an explicit dynamic calculation method, with automatic surface-to-surface contact established between the rock

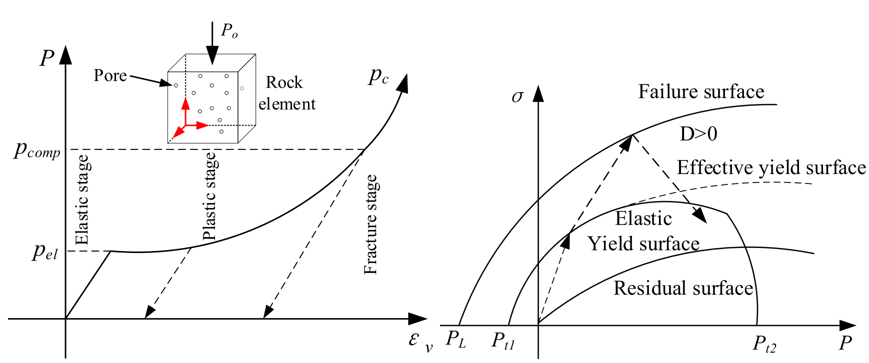

(a) Pore crushing pressure and volumetric strain (b) Stress limit surfaces and loading scenario

Fig. 5. Riedel Hiermaier Thomas model principle.

specimen and rigid plates. The bottom rigid plate is fully constrained with fixed boundary conditions, while the top rigid plate applies a controlled compressive load at a constant velocity of 0.1 mm/s. In accordance with the GB/T 50218–2014 standard, the rock specimens are prepared with specific dimensions: cylindrical samples of 50 mm in diameter and 100 mm in height for uniaxial compression tests, and disk-shaped samples of 50 mm in diameter and 25 mm in thickness for Brazilian splitting tests. The mesh size of the rock sample is 1 mm. The Riedel Hiermaier Thomas model incorporates a total of 38 parameters, among which only those exerting significant influence on the numerical simulation of tool-induced rock fragmentation are calibrated in this study. The remaining parameters are primarily derived from relevant literature and will be finalized through fine-tuning and experimental validation. The f_c, f_t^*, and f_s^* have the greatest impact on rock stress, among which $f_t^* = f_t/f_c$, $f_s^* = f_s/f_c$. The tensile strength of rocks is usually one-tenth of their compressive strength, and the shear strength is one-fifth of their compressive strength. The elastic shear modulus G, p_{el}, p_{comp} mainly affects the slope of the stress curve. The parameters of A, N, A_f, and n_f affect the damage of rocks.

As shown in Fig. 6, the peak stress of the rock measured in the numerical simulation is very similar to the results obtained in the engineering experiment, and the stress-strain curve and fracture effect of the rock in the numerical simulation conforms to the conventional fracture types of the rock. It should be noted that the RHT model focuses more on the inelastic behavior of the model, which is ideally linearly elastic in the pre-stress period. However, the experimental elastic modulus is very sensitive to microcrack closure effects during initial loading. As a result, there is some deviation in the slope of the first half of the stress-strain curve between numerical simulation and experiment. The rock in the Brazilian splitting experiments was mainly subjected to tensile stresses, and there was no initial fracture closure. Therefore, the fracture characteristics of the rock (Red damage shape) in the Brazilian splitting test are almost consistent with the engineering experiment. This proves that the rock parameters calibrated in this study can accurately characterize the process of rock fragmentation. The rock parameters are shown in Table 1. Notably, the overall compressive strength of the rock is 142 MPa and the tensile strength is 10.9 MPa. The compressive strength of the high-hardness minerals in the granite component is 167.8 MPa, the shear strength is 35.24 MPa, and the tensile strength is 6.7 MPa. The compressive strength of medium-hardness minerals is 119 MPa, the shear strength is 21.42 MPa, and the tensile strength is 11.9 MPa. The compressive strength of low-hardness minerals is 48 MPa, the shear strength is 11.52 MPa, and the tensile strength is 4.8 MPa. Hardness is an intrinsic property of minerals and is more representative of the compositional classification of minerals, whereas strength is better suited to describe the macroscopic mechanical properties of minerals. Thus, hardness is used to describe the compositional classification of minerals, while strength is used to describe the compressive strength of minerals.

To further validate the capability of the numerical model developed in this study in accurately simulating the rock fragmentation process under tool impact, a simulation of rock breaking by the three commonly employed tools in engineering applications was conducted based on the model parameters presented in Table 1 and the previously described heterogeneous rock modeling methodology. The scientific validity of the numerical model was systematically verified through a comparative analysis of the rock fragmentation characteristics between simulation results and experimental observations. As shown in Fig. 7, under the same conditions, the consistency between the experimental and simulated rock-breaking characteristics of the tool impact is high. Both numerical simulations and experimental results demonstrate that the fracture patterns induced by type A and type C tools exhibit a distinct cross-shaped morphology during rock breaking. In contrast, the type C tools produce linear fracture patterns. Notably, comparative analysis reveals that type C tools, due to their larger contact area with the rock surface, generate more extensive damage zones compared to type A tools. The comparative results between experimental data and numerical simulations of tool-impact rock fragmentation demonstrate that the proposed model in this study accurately reproduces the actual rock-breaking process under impact conditions.

3. Results and discussions

3.1. Analysis of rock breaking process by tool impact

From a macro perspective, the impact hammer impacts the tool at high speed and loads the impact energy onto the rock, leading to rock fragmentation. However, analyzing the rock-breaking process of the tool at a smaller time scale reveals that during a single impact by the impact hammer, the impact velocity and displacement of the tool undergo multiple changes. As shown in Fig. 8, the displacement and velocity variation trends of b-type cutting tools and hammer during rock breaking under different impact kinetic energy conditions. The initial velocity of hammer V1 is equal to 5.4 m/s, V2 is equal to 10 m/s. During the rock-breaking process of the tool, the displacement and velocity of the impact hammer are always vertically downward along the Y-axis, while the magnitude of the velocity direction of the tool during a single impact rock-breaking process constantly changes. The tool repeats the process of impact rebound impact in the Y direction. However, this repeated impact rebound impact motion behavior only exists when the impact hammer speed is small (the impact force is not enough to break the adhesion between rock particles in one go). If the speed of the impact hammer is very high, the impact force generated by the tool hitting the rock instantly reaches or far exceeds the mechanical performance standards for rock fragmentation. The repeated collision between the tool and the impact hammer causes the velocity curve of the impact hammer to decrease in a stepped shape, and it can be seen from the graph that the velocity change of the tool becomes more pronounced

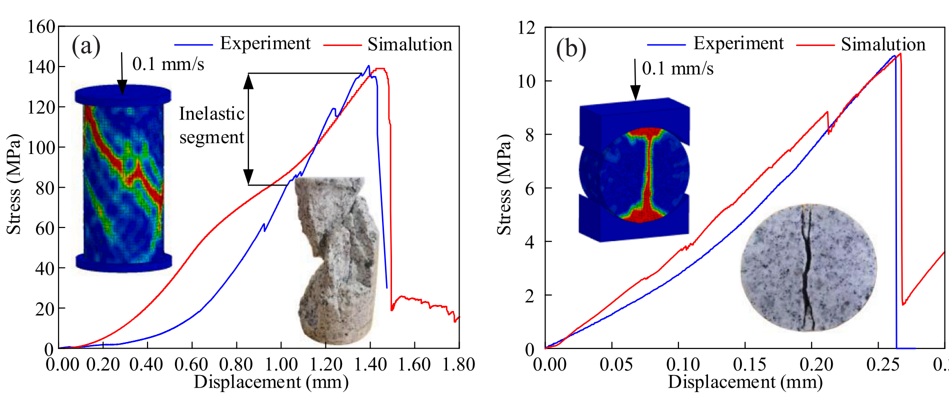

Fig. 6. Experimental and simulation comparison of rock compression and tension: (a) uniaxial compressive strength; (b) brazilian split test.

Table 1
Constants summary of Riedel Hiermaier Thomas model for granite [38–40].

Parameter	50% Quartz	45% Feldspar	5% Mica	Parameter	50% Quartz	45% Feldspar	5% Mica
ρ(kg/m^3)	2660	2700	2600	ε_p^m	0.015	0.012	0.010
α_0 (%)	0.0	0.0	1.08	Q_O	0.68	0.64	0.70
p_{el} (Pa)	1.25×10^8	4.00×10^7	1.60×10^7	D_1	0.040	0.042	0.040
p_{comp} (Pa)	6.0×10^9	5.5×10^9	6.0×10^9	D_2	1	1	1
G(GPa)	21.90	24.17	8.00	A	2.44	1.60	1.65
f_c(MPa)	167.8	119.0	48.0	N	0.76	0.61	0.56
f_t^*	0.04	0.10	0.10	A_f	0.25	1.62	1.59
f_s^*	0.21	0.18	0.25	n_f	0.62	0.60	0.62
$\dot{\varepsilon}_c^0$ (ms^{-1})	3×10^{-8}	3×10^{-8}	3×10^{-8}	$\dot{\varepsilon}_c$(ms^{-1})	3×10^{22}	3×10^{22}	3×10^{22}
$\dot{\varepsilon}_t^0$(ms^{-1})	3×10^{-9}	3×10^{-9}	3×10^{-9}	$\dot{\varepsilon}_t$(ms^{-1})	3×10^{22}	3×10^{22}	3×10^{22}
B	0.050	0.105	0.105	n	3	4	3

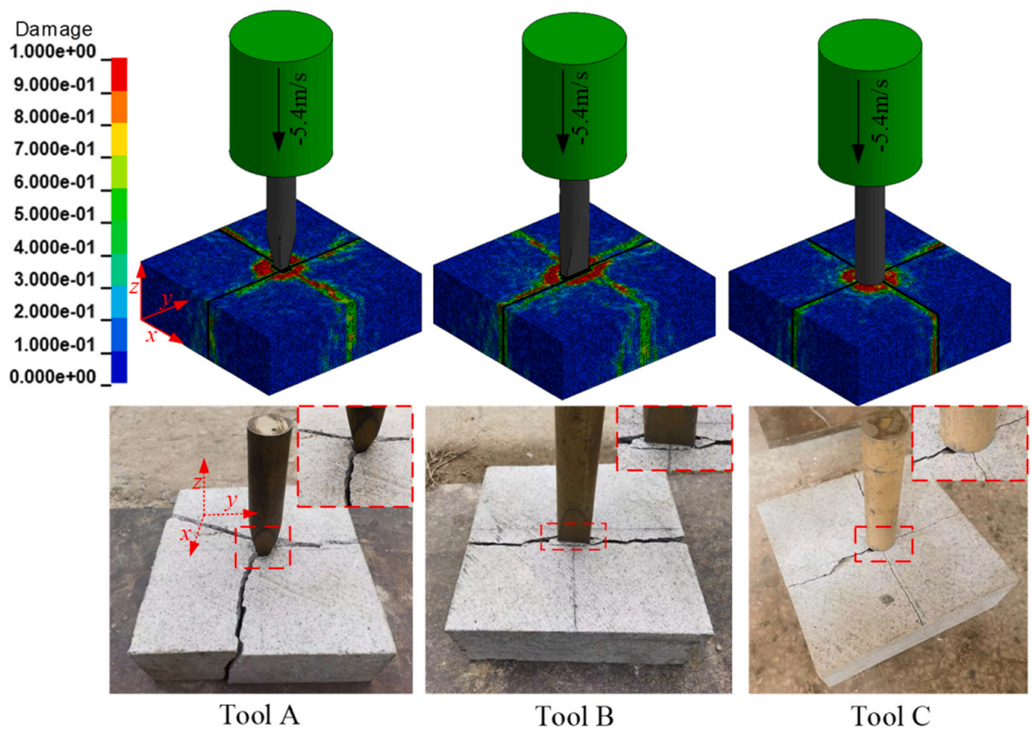

Fig. 7. Experimental and simulation comparison of rock breaking with tool impact.

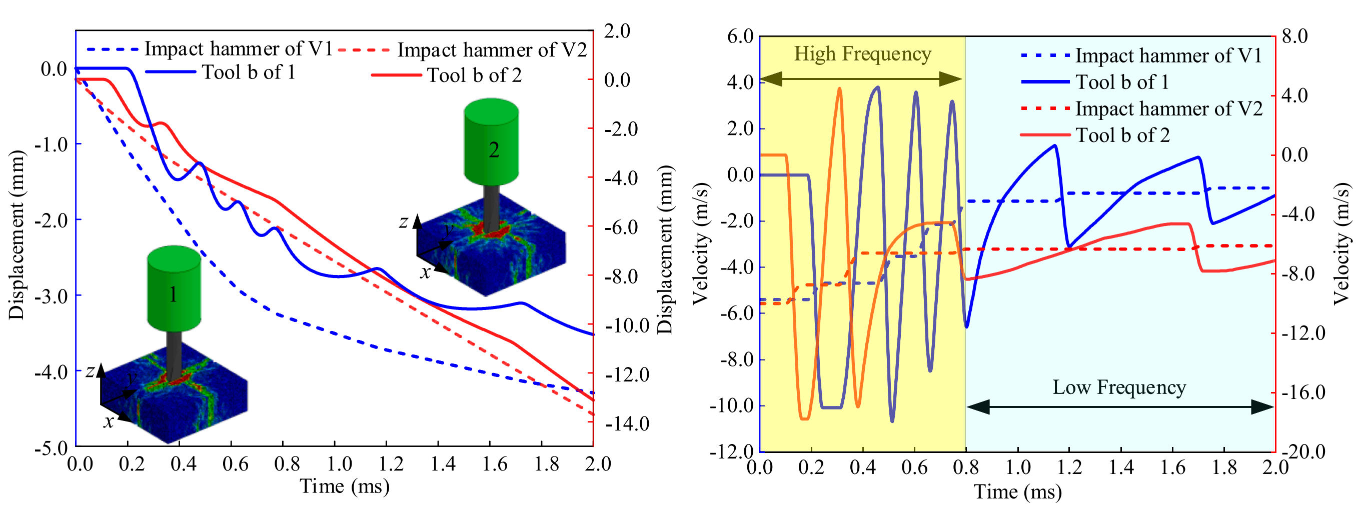

(a) Displacement curve (b) Velocity curve

Fig. 8. Displacement and velocity curves of impact hammer and tool.

when the initial kinetic energy of the impact hammer is relatively low. The process of rock breaking by the tool is only completed when the final velocity of the tool and the impact hammer becomes consistent.

A rock section is intercepted to analyze the relationship between stress and damage, and the bottom of the rock is constrained to move in the Z direction in the numerical model. As shown in Fig. 9, the black arrow line should indicate the transition of the rock from compression to tension, while the red arrow should indicate the transition of the rock from tension to compression. From the perspective of the impact motion behavior of the tool, the damage and stress evolution process of heterogeneous rock sections can be divided into four stages, namely impact-rebound and impact-rebound. The impact of the tool on the rock instantly generates a certain stress wave, which spreads in a circular arc towards the interior of the rock with the impact point as the center. Due to the continuous diffusion of stress waves along the depth direction of the rock, their distribution within the rock cross-section is approximately fan-shaped. The damage degree of homogeneous rock under the impact of cutting tools is relatively high, resulting in the formation of fracture pits at the impact point of the last stage, and no rebound occurs. Therefore, the stress division of homogeneous rocks does not include the fourth stage (transition from compression to tension).

At 324 μs, stress waves spread towards the interior of the rock around the impact point. The difference between heterogeneous rocks and homogeneous rocks is that the edges of the stress layer in heterogeneous rocks are not smooth, and there is a phenomenon of cross-layer stress distribution. The damaged elements are mainly located at the edge of the stress layer. As the depth of stress wave propagation increases, the energy of stress waves continuously decays, thereby reducing the stress difference at the edge of the stress layer until it is insufficient to cause rock damage. This is also the main reason why the damage distribution in various rock cross-sections decreases continuously along the direction of stress transfer during the early stage of stress wave propagation (324-364 μs).

At 339 μs, stress waves propagate to the bottom of the rock and begin to propagate in the opposite direction with the corresponding position of the impact point at the bottom of the rock as the center of the circle. At 364 μs, the stress wave transmitted in the reverse direction overlaps with the stress wave transmitted in the forward direction. From the stress color, the stress transmitted in the reverse direction is smaller than that transmitted in the forward direction. Therefore, when the forward and reverse stress waves meet, the overall transmission direction of the stress wave is not changed, but rather the shape of the stress wave transmission process is changed. Moreover, the cross-layer distribution of stress in heterogeneous rock interfaces is more severe. At this point, due to the influence of backpropagation stress, the position and size of the original stress layer boundary have changed. Under the influence of existing damage, newly generated damage begins to exhibit complexity, but the overall distribution of damage still conforms to the approximate shape of the stress boundary.

At 451 μs, the first impact process of the tool ends and begins to enter the rebound stage. The impact position of the tool is no longer transmitting compressive stress waves to the interior of the rock, and the already generated stress waves gradually dissipate during the transmission process. A point-like distribution of damage begins to appear below the impact point of the non-uniform rock at this moment, and multiple fine cracks appear at the boundary of the original stress layer. At 506 μs, the tool detaches from the rock, and the stress within the rock section is fully dissipated. The stress borne by the rock element directly below the impact point appears as a fault. At this point, the rock element located below the impact point within the rock cross-section generates a layered damage zone. The degree of damage inside heterogeneous rocks is relatively low, but the distribution of damage between layers is denser. By comparing the distribution of damage within the rock cross-section during the impact stage, it can be concluded that the generation of rock damage mainly occur through the process of stress dissipation. At 563 μs, the rebounded tool struck the rock again, further exacerbating the damage to the already damaged rock elements, making the distribution of cracks in the rock section more pronounced. From the graph, the distribution of radial stress waves inside heterogeneous rocks are finer, and the significance of stress differences between layers gradually decreases. This phenomenon explains why the degree of damage inside heterogeneous rocks is relatively low compared to homogeneous rocks, while the range of damage is relatively large.

As the tool is continuously pressed down, the stress amplitude

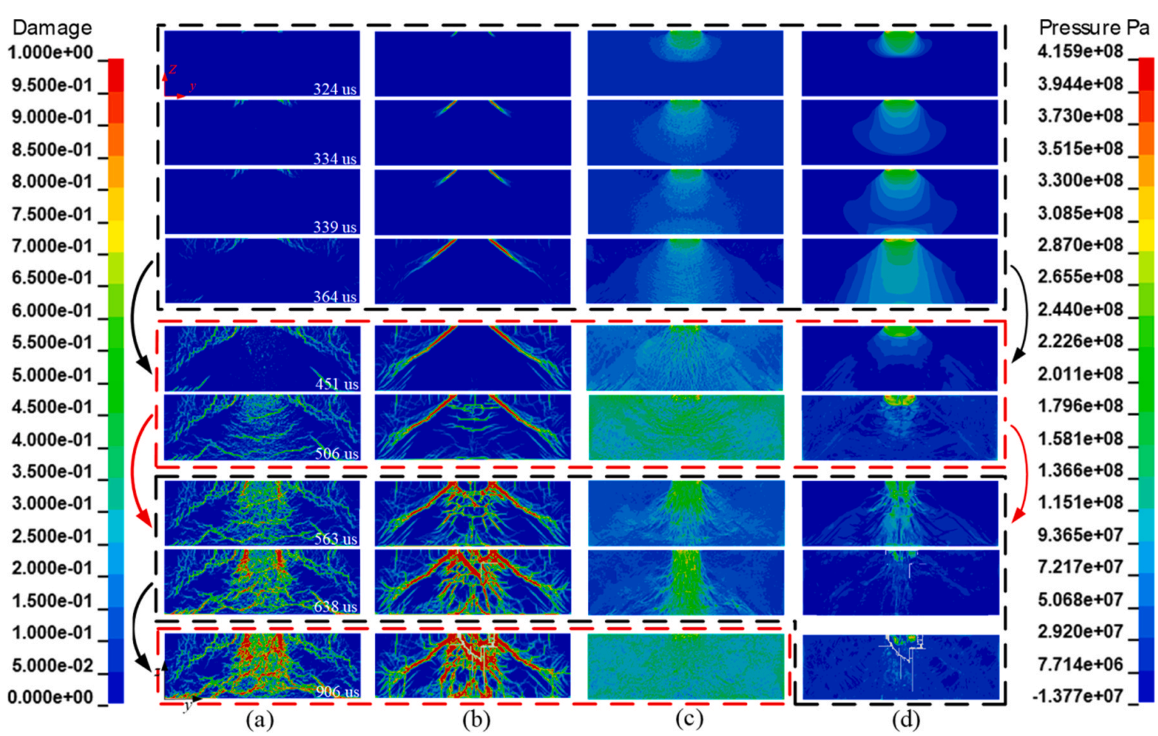

Fig. 9. Cloud chart of rock section damage and stress evolution.

generated by the impact correspondingly increases. From the stress distribution inside the heterogeneous rock at 638 μs, the stress value below the main impact point significantly increases, and there is a significant layering with the surrounding rock. This phenomenon causes an increase in the degree of damage to the rock elements along the stress stratification edge inside heterogeneous rocks. The continuous downward pressure of the tool increases the stress difference at the edge of the stress layer inside the homogeneous rock. The damage to rock elements further intensifies, leading to the deletion of some elements. The deleted rock section of the element generates a free surface, which accelerates the dissipation of stress waves. This is the main reason for the relatively small area of stress distribution within the homogeneous rock section at 638 μs. At 906 μs, the kinetic energy of the tool is almost completely lost, and the damage within the rock section is basically fixed. From the damage cloud map, the degree of damage inside the rock deepens during the second rebound stage, and the damage distribution does not undergo significant changes.

3.2. Analysis of rock breaking mechanism by tool impact

During the process of impacting and breaking heterogeneous rocks, rock elements undergo complex stress changes. Exploring the underlying causes of triggering rock failure and removal is crucial for improving the efficiency of hard rock fragmentation and creating reasonable fracture characteristics of rocks. The impact rock-breaking mechanisms of different tooth-shaped tools are similar. To avoid repetitive work, this article takes the flat tool impact rock-breaking process as the research object, extracts the stress and damage change curve of the rock, and deeply analyzes the main factors that cause rock fragmentation under mechanical impact rock-breaking conditions. As shown in Fig. 10, extract the stress curves of the flat tool fracture surface and its rock elements on both sides. The maximum principal stress and minimum stress are positive values, indicating that the rock element is subjected to tensile stress, while their amplitude represents that the rock element is subjected to compressive stress. The tool impact rock breaking cloud diagram in Fig. 10c indicates the location of the extracted stress rock elements, where H101151 is the rock element at the fracture site, and H102751 and H99551 are the rock elements with lower damage on both sides of the fracture surface. The light-yellow area in the figure (cumulative damage) is determined based on the cumulative damage area of the rock element in Fig. 10b. From Fig. 10b, the rock elements did not show any damage before 0.5 ms, and gradually accumulated damage between 0.6 ms and 0.8 ms. Especially when element H101151 approaches 0.8 ms, its damage value rapidly accumulates and reaches complete damage. From this, it can be inferred that factors leading to rock fracture and failure occurred near the time of 0.8 ms. From Fig. 10a, the peak tensile stress borne by the rock elements on the fracture surface is much greater than that of the rock elements that have not undergone failure or deletion at the edge of the fracture surface, and greater than the ultimate compressive strength of high-strength minerals in heterogeneous rock composition. Based on this, it is preliminarily determined that the tensile stress induced by the impact of the tool on

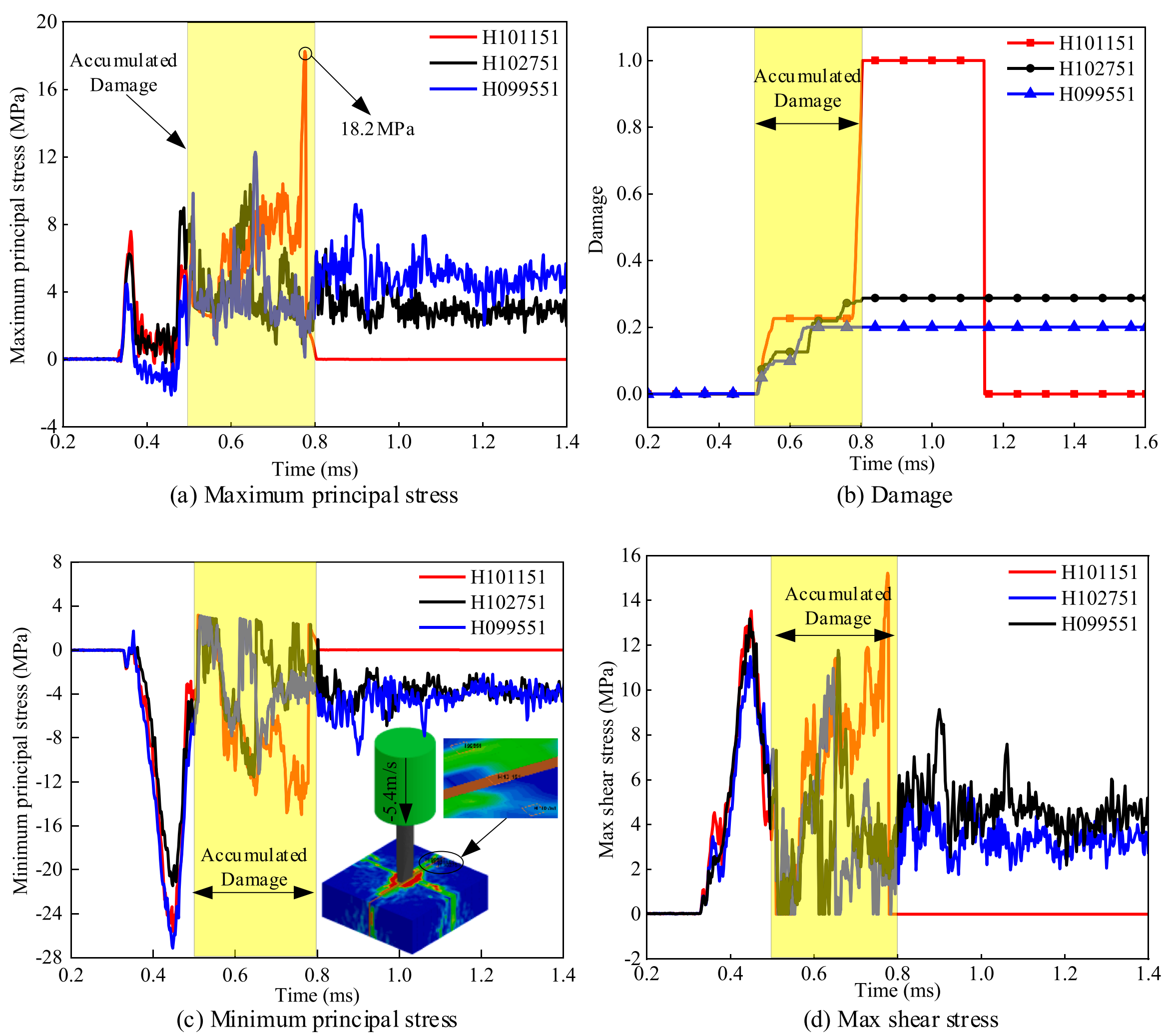

Fig. 10. Damage and stress curves of the fracture surface and its adjacent elements.

the rock is the main factor leading to rock fracture. In Fig. 10c, the compressive stress borne by rock element H101151 within the cumulative damage interval of the rock element is greater than that of H102751 and H99551. However, this does not indicate that the compressive stress induced by tool impact is the main cause of rock fracture and fragmentation. Before the cumulative damage area, the rock element bears a relatively large compressive stress, and the compressive stress borne by the H99551 element is slightly greater than that of the H101151 element. However, no damage occurred to the rock elements within the time domain of the peak compressive stress. Moreover, the peak compressive stress is much smaller than that of the mineral with the lowest uniaxial compressive strength in heterogeneous rock composition. From this, it can be concluded that the compressive stress generated by the tool impact is not the main cause of rock fracture and fragmentation. The trend of the shear stress curve of the rock element in Fig. 10d is like that of the minimum principal stress curve, and there is also a large stress peak before the cumulative damage area of the rock element. However, this does not indicate that shear stress is not the cause of rock fracture and fragmentation. Because the peak shear stress borne by rock element H101151 in the cumulative damage area is relatively large and greater than the ultimate shear strength of the mineral with the lowest strength in the heterogeneous rock composition. The rock has a relatively low proportion of low-strength minerals, and the cumulative damage zone also has a relatively low peak shear stress. From this, it can be concluded that the contribution of shear stress generated by tool impact to rock fracture is lower than that of tensile stress but higher than that of compressive stress.

As shown in Fig. 11, H109380 and H101151 are rock elements taken from the fracture surface, while H76711, H76373, H93001, and H93021 are rock elements taken from the damage zone perpendicular to the fracture surface. From Fig. 11a, the peak tensile stress borne by rock elements H109380 and H101151 is larger than that of rock elements H93001 and H76711. From the damage accumulation curve in Fig. 11b, the damage accumulation speed of the rock element at the fracture surface is faster, and it has been deleted before the rock element in its vertical direction reaches the complete damage or shear failure standard. Based on this, it can be concluded that the non-uniform distribution of tensile stress induced by tool impact in the direction of vertical tooth width and along the tooth width is one of the reasons for rock fracture along the tooth width direction. Extracting the maximum principal stress curves of rock elements at the fracture surface and its vertical direction multiple times, it was found that not all rock elements in the vertical tooth width direction have a lower maximum principal stress than those along the tooth width direction. Moreover, there are also rock elements that achieve complete damage perpendicular to the tooth width direction. As shown in Fig. 11c, there is no significant difference in the maximum principal stress curve corresponding to rock elements at different positions. However, this cannot deny that tensile stress is the main cause of rock fracture and failure, as well as the judgment that the tensile stress induced by tool impact on the rock has a larger component along the tooth width direction. Reason 1: All rock elements in Fig. 11d have achieved complete damage. This proves that

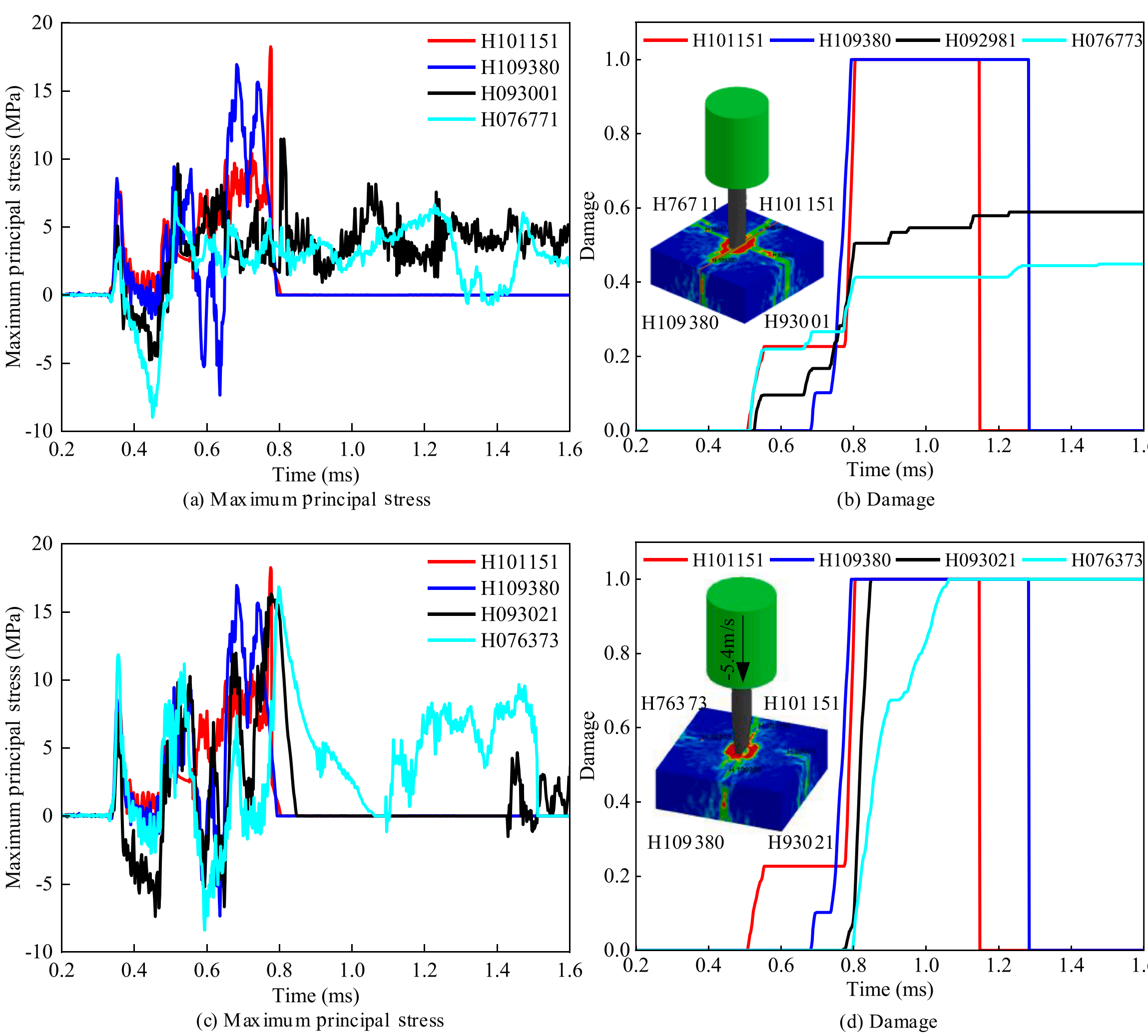

Fig. 11. Maximum principal stress and damage curve of rock elements at vertical damage location.

tensile stress is indeed the main cause of rock damage and failure. Reason 2: From the rock damage distribution map at 0.77 ms in Fig. 11d, the speed at which the rock elements along the tooth width direction reach complete damage is generally greater than that perpendicular to the tooth width direction. In addition, the stress fluctuations of the rock elements in Fig. 11c almost occur at the same time. This can exclude the issue of the propagation speed of tensile stress induced by tool impact. Based on the above analysis, it can be concluded that the overall tensile stress induced by tool impact is relatively large along the tooth width direction. The phenomenon in Fig. 11c indicates that the conclusion that the tensile stress induced by rock breaking by tool impact has a larger component along the tooth width direction is an overall trend, rather than the fact that the tensile stress along the tooth width direction is greater than that of the rock element perpendicular to the tooth width direction. From the rock damage curve in Fig. 11d, the damage generation time and deletion speed of the rock elements at the fracture surface are earlier than those at the vertical fracture surface. This phenomenon corresponds to the ultimate fracture characteristics of the rock. Based on the above analysis, it can be concluded that the distribution of tensile stress and the cumulative velocity of damage along the rock's anisotropy are the main factors determining the macroscopic fracture characteristics of rocks.

The instantaneous impact point of the tool on the rock and the tensile, compressive, and shear stress values borne by the surrounding rock elements are relatively large, and the damage and failure mechanism of the rock is more complex. Studying the damage and failure mechanism of rock elements at the impact point of the tool is beneficial for creating a reasonable shape of the fragmentation pit and improving the efficiency of rock fragmentation in practical engineering. As shown in Fig. 12, element H116961 is extracted from the center of the impact point on the surface of the rock. The yellow area in the figure represents the cumulative area of rock element damage. From the stress curve in the figure, the rock element at the impact point hardly bears tensile stress during the entire rock-breaking process of the tool but bears relatively large shear and compression stresses, and the peak values of shear and compression stresses are far greater than the ultimate shear and compression strength of high-hardness minerals in heterogeneous rocks. Moreover, the shear stress of element H116961 and the peak stress of the minimum principal stress are almost at the same time. From this, it can be preliminarily determined that compression and shear stress are the main causes of rock failure at the mechanical impact point. It is worth noting that the cumulative damage process of the rock element at the impact point mainly occurs in the time after the peak of compression and shear stress, and the cumulative time is very short.

As shown in Fig. 13, extract the average stress curves of four rock elements in the damaged area around the impact point, and plot the

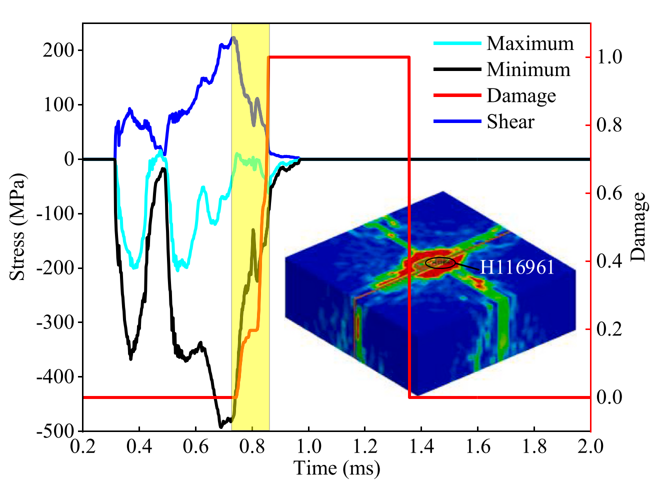

Fig. 12. Stress and damage of rock elements at the impact point.

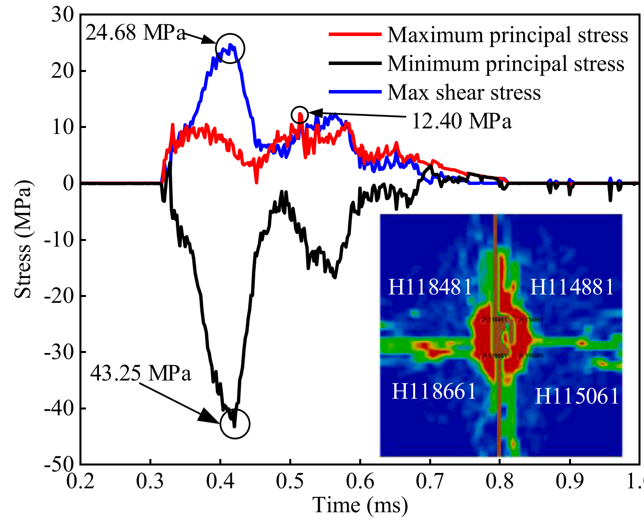

Fig. 13. Stress curve of rock elements around the impact point.

variation curves of different stresses over time. Based on Fig. 13, the compressive stress borne by the rock around the impact point of the tool is relatively low, and the peak stress is still lower than the compressive strength of the mineral with the lowest strength in heterogeneous rocks. Unlike the stress distribution of rock elements at the center of the impact point, tensile stress occurs in the surrounding rock elements, and the peak stress is greater than the overall tensile ultimate strength of heterogeneous rocks. Although the peak shear stress of the rock elements around the impact point is relatively low, it still reaches the shear limit of some minerals in heterogeneous rocks. From this, it can be preliminarily determined that tensile stress and shear stress are the main causes of damage to the rock elements around the impact point (not directly in contact with the tool).

As shown in Fig. 14b, the damaged rock element numbers include H115061, H114841, 118861, and H118281, while the undamaged rock element numbers include H113481, H114841, H118861, and H118281. From the figure, the average values of tensile stress, shear stress, and compressive stress borne by the damaged element during the cumulative damage stage are greater than those of the undamaged rock element. Further analysis shows that from Fig. 14a, the average tensile stress value of the damage element during the damage accumulation stage not only has a relatively large overall amplitude but also the peak stress fluctuates near the tensile limit of heterogeneous rocks. From this, it can be determined that the tensile stress induced by mechanical impact is the main reason for the failure of rock elements around the impact point. Based on the variation pattern of the cumulative damage curve in Fig. 14b, it can be concluded that, unlike the previous analysis of the damage mechanism of rock elements at the fracture surface, the damage of rock elements around the impact point mainly occurs in the stress reduction stage after the peak tensile stress. Moreover, in Fig. 14c-d, the late stage of damage accumulation (rapid damage accumulation) corresponds to the stress reduction stage after the peak of shear and compressive stress. This phenomenon is similar to the damage and failure pattern of rock elements at the impact point. The peak shear stress of the rock element in Fig. 14c is close to 25 MPa, which has exceeded the tensile limit of medium-strength mineral in non-mean rocks (21.42 MPa). The peak shear stress of undamaged rock elements is much lower than the ultimate shear strength of 95% mineral in heterogeneous rocks. This can once again demonstrate that shear stress is indeed one of the reasons for the damage and failure of rock elements around the impact point. Although the average compressive stress of the damaged rock element in Fig. 14d is greater than that of the undamaged rock element, it does not indicate that compressive stress plays a role in the damage process of the rock element around the impact point. Not

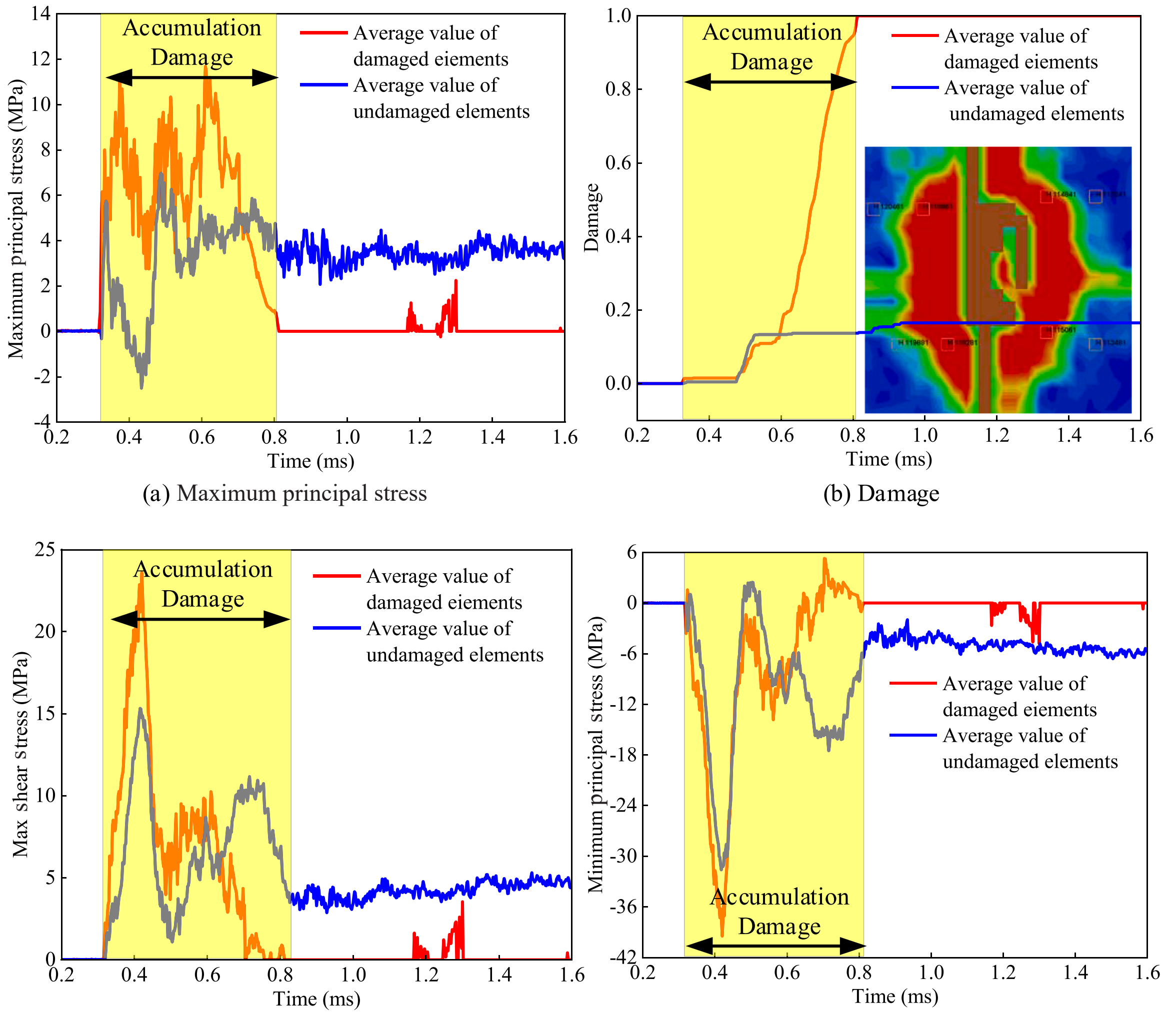

(a) Maximum principal stress
(b) Damage
(c) Max shear stress
(d) Minimum principal stress

Fig. 14. Stress and damage curves of damaged and undamaged rock elements around the impact point.

only because the compressive stress borne by the damaged element is much lower than the ultimate compressive strength of heterogeneous rocks. Another reason is that the compressive stress borne by some undamaged rock elements is greater than that of the damaged elements.

Cut the rock model along the fracture surface and extract the stress curve of the rock elements in the longitudinal section of the rock. Analyze the internal stress distribution of the rock along the direction of the tool impact, and divide the failure zone of the rock element based on the ultimate crushing strength of heterogeneous rocks. As shown in Fig. 15, the extracted rock elements are H116561, H116565, H16569, and H16573 from top to bottom.

From Fig. 15a-b, the rock elements below the impact point bear very high compressive and shear stresses, far exceeding the compressive and tensile limits of heterogeneous rocks. The selected rock section is close to the fracture surface. Therefore, it can be seen from Fig. 15c that the rock element below the impact still bears a certain amount of tensile stress at special moments, but still mainly relies on compression and shear. Based on the comprehensive analysis of Fig. 15a-c, it can be concluded that as the impact depth increases, the compressive and shear stresses borne by the rock rapidly decrease, while the tensile stress it bears gradually dominates in the fractured rock. It is worth noting that the amplitude decrease of the shear stress curve is lower than that of the compression stress, and it still can break rocks at a certain depth of damage. From the damage curve of the rock element in Fig. 15d, the closer to the impact point of the tool, the faster the rock damage speed. The further away from the impact point, the more complete the damage of the rock element needs to go through multiple stepped accumulations. Moreover, the further away the rock element from the impact site of the tool, the longer it takes for the damage to accumulate and reach complete damage.

Extract the stress curve of the rock element below the non-impact point in the longitudinal section of the rock, and analyze the reasons for the failure of the rock at the internal fracture surface of the rock. As shown in Fig. 16a-c, the peak shear stress borne by the rock element (not below the impact point) in the internal section of the rock is less than 16 MPa, and the compressive stress is less than 24 MPa. Not only is it much lower than the macroscopic ultimate compressive and shear strength of heterogeneous rocks, but its stress peak is still not enough to crush the mineral with the lowest hardness in the composition of heterogeneous rocks. However, from Fig. 16c, the tensile stress borne by the rock is relatively high compared to the macroscopic tensile strength of the rock, and some rocks bear much higher tensile strength than the high-strength mineral in heterogeneous rocks. Of course, there are also a few elements in the longitudinal section that are less affected by the impact of tooling. However, this does not affect the overall fracture characteristics of the rock. As shown in Fig. 16, the rock element numbered H100536 bears compressive, shear, and tensile stresses that reach the ultimate damage strength of heterogeneous rocks. However, most of the rock elements located within the same section have already been damaged and failed, and the rock will still split along this section.

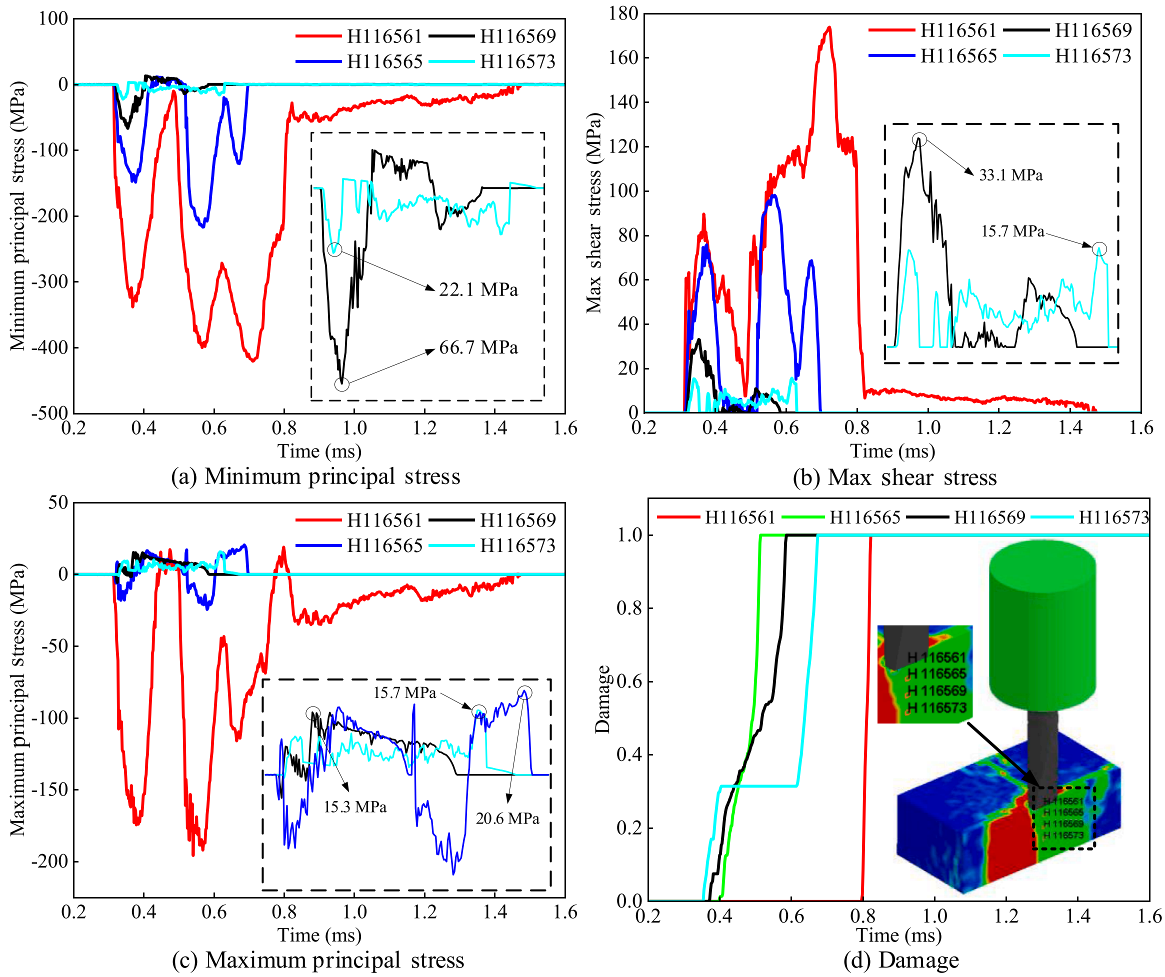

(a) Minimum principal stress (b) Max shear stress (c) Maximum principal stress (d) Damage

Fig. 15. Stress and damage diagram of the rock element below the impact point in the longitudinal section of the rock.

In summary, the damage areas after tool impact rock breaking can be roughly divided based on the dominant factors of rock damage in different regions. The cross-section can be divided into compression shear stress dominant zone and tension shear dominant zone. The former has a high stress value and forms a fracture pit at the impact point, while the latter has a lower stress value but causes rock fracture and failure. From the impact point downwards, the vertical section of rocks can be divided into the dominant zone of compressive shear stress, the transitional zone of multiple factors, and the dominant zone of tensile shear stress.

3.3. The influence of confining pressure on mechanical impact rock breaking

Improving the efficiency of hard rock fragmentation under confining pressure conditions is a key technical problem that urgently needs to be overcome in deep coal energy mining. Studying the damage distribution and rock fragmentation mechanism of mechanical impact fragmentation of heterogeneous rocks under confining pressure can provide certain assistance for improving rock fragmentation efficiency in practical engineering applications. As shown in Fig. 17, the surface pressure is applied around the rock to simulate the true confining pressure state of the rock in a deep ground environment. It can be seen from the overall damage distribution of the rock that the damage range of the rock gradually narrows with the increase of confining pressure, especially the length of cracks, and their degree of damage significantly decreases. Although the damage distribution of the rock is still very significant under a confining pressure of 1 MPa, macroscopic fracture effects cannot be formed after the impact of the tool. When subjected to a confining pressure of 2 MPa, the degree of damage to the rock element at the crack location decreases, and the crack in the vertical tooth width direction has begun to exhibit discontinuities. When subjected to a confining pressure of 3 MPa, the damage distributed in the vertical tooth width direction completely disappears, and the degree of damage to the rock elements at the crack location along the tooth width direction further decreases. When subjected to a confining pressure of 4 MPa, the damage on the rock surface along the tooth width direction gradually disappears, and the damage to the rock element at the impact point begins to attenuate. Until the confining pressure of 5 MPa was applied, the damage distribution on the rock surface completely disappeared, and the damage distribution range of the rock element at the impact point further narrowed. When the confining pressure is greater than 5 MPa, the cracks on the surface of the rock completely disappear; only at the impact point is there damage, and the damage distribution range is basically not changing. Therefore, this section mainly analyzes the damage evolution law of rocks within the range of 5 MPa. From the changes in the distribution of rock surface damage during the increase of loading confining pressure, the presence of confining pressure significantly suppresses crack and damage propagation, and its impact on crack propagation is more significant. Based on the conclusion in Section 3.2, it can be concluded that the presence of confining pressure has the greatest impact on the propagation of tensile stress during mechanical impact.

Due to the influence of the weight of overlying rock layers and the tectonic movement of geological plates, the confining pressures borne by deep rock masses are not equal in all directions. The ratio of

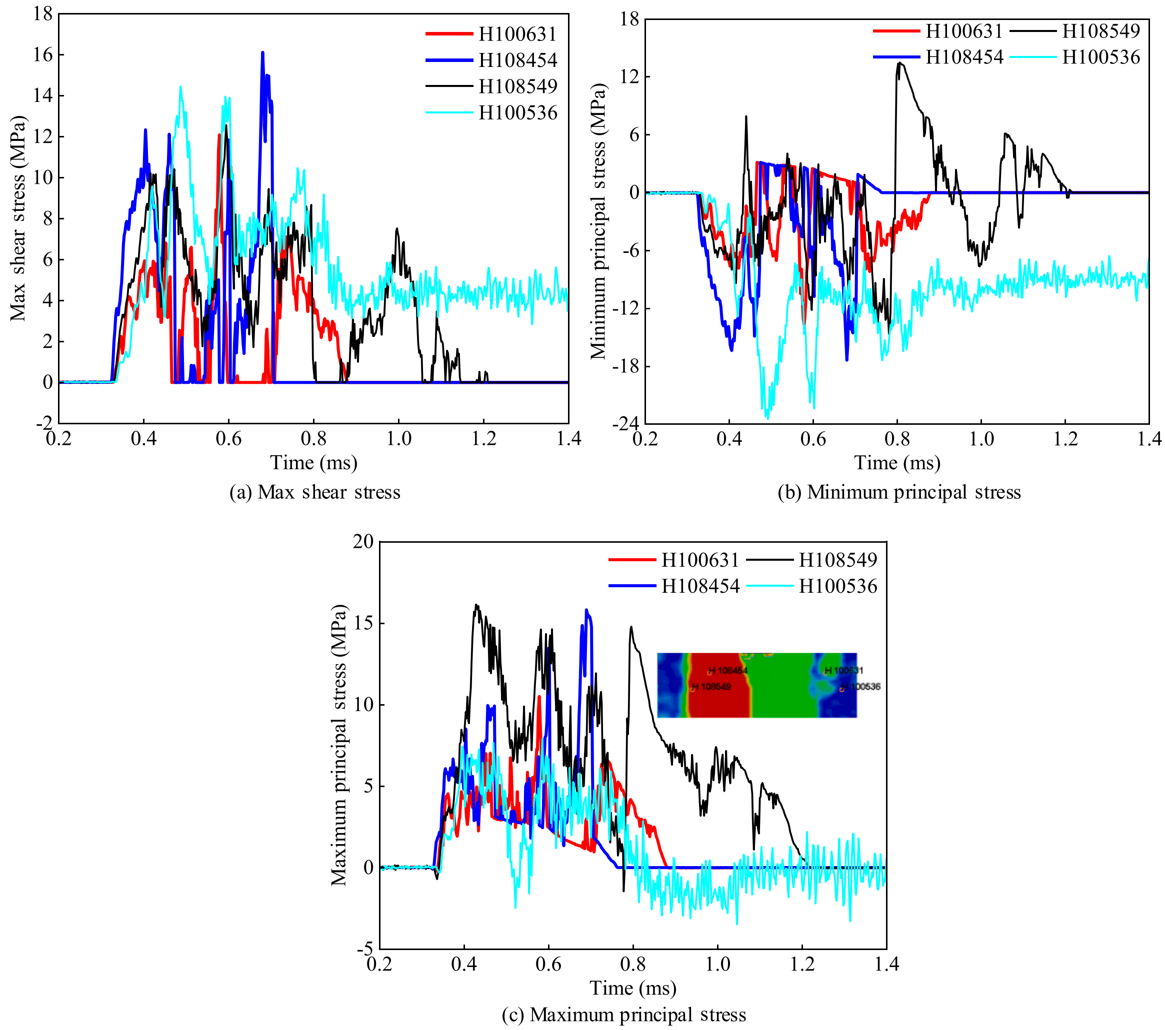

(a) Max shear stress (b) Minimum principal stress

(c) Maximum principal stress

Fig. 16. Stress and damage diagram of the outer edge rock element in the longitudinal section of the rock.

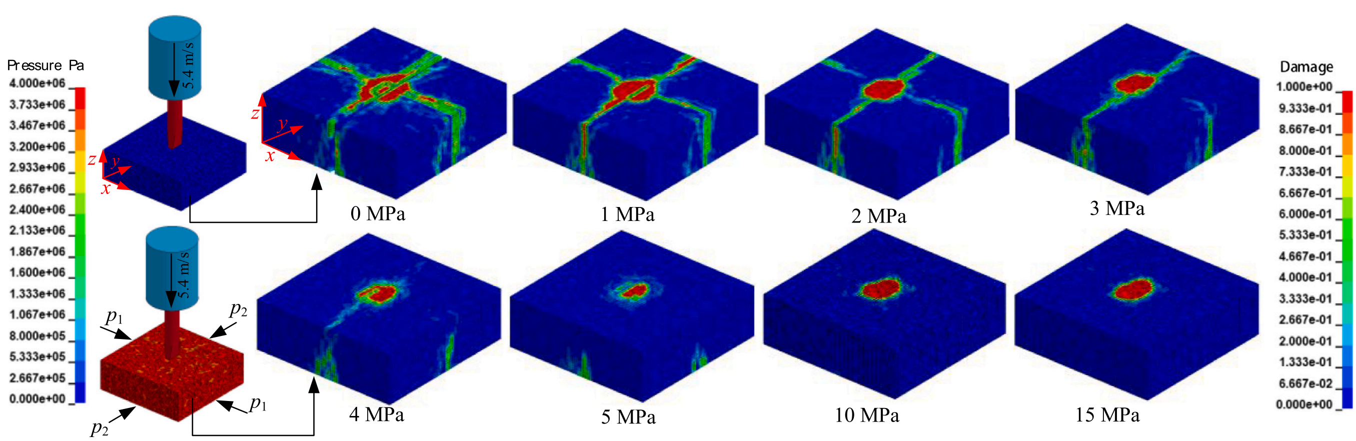

Fig. 17. Damage distribution of rock fragmentation by tool impact under different confining pressures.

horizontal confining pressure F_h to vertical stress F_v is between 0.8 and 1.5, and the horizontal stress is generally greater than the vertical stress. In numerical simulation, the horizontal stress is taken as 1.2 times the vertical stress to analyze the distribution of damage after the tool impacts the rock [41,42]. As shown in Fig. 18, when the tooth width of the tool is parallel to the horizontal confining pressure, the impact rock damage of the tool is less affected by the confining pressure. When the tooth width direction is perpendicular to the horizontal confining pressure, the damage to the rock surface significantly decreases. From this, it can be concluded that the rock is more prone to fracture and failure along the direction of maximum surrounding rock stress during the process of breaking through the rock with a tool under confining pressure. In practical engineering, the impact direction of the tool can be quickly adjusted according to the rock confining pressure state,

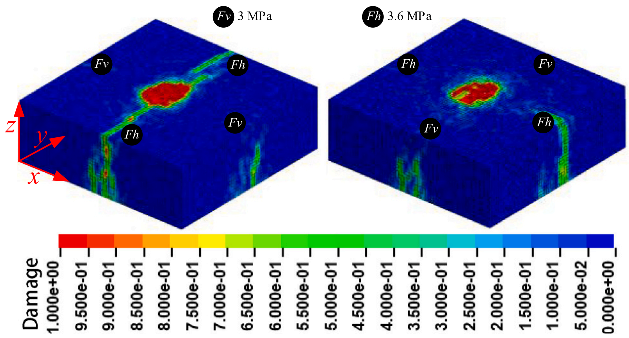

Fig. 18. Effect of confining pressure loading direction on the distribution of rock damage caused by tool impact.

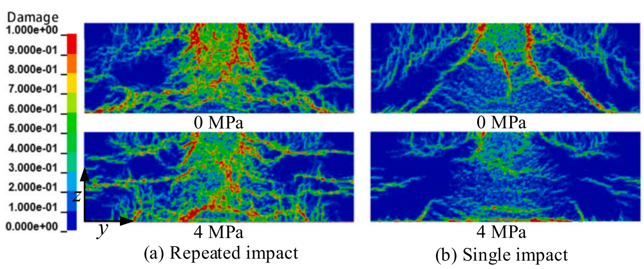

Fig. 19. Distribution of rock section cracks under different confinement pressures.

accelerating the crushing efficiency of high-hardness rocks under confining pressure.

During a single impact of the impact hammer, the tool impacts the rock multiple times, and after multiple damages, the cracks in the rock section are very complex. To highlight the influence of confining pressure factors on the distribution of internal cracks in rocks, the damage distribution of the cross-section after single and multiple impacts of the tool is taken to comprehensively analyze the influence of confining pressure factors on the propagation of internal cracks in rocks. As shown in Fig. 19, the overall damage degree of internal cracks in the rock under confining pressure loading is relatively low, and the cracks tend to be distributed along the horizontal direction, this situation is more significant in the section where the rock is broken by a single impact of the tool. Moreover, there are relatively few branching cracks at the edge of the main crack in the rock section under confining pressure. Based on the previous conclusion (tensile stress and shear stress are the main causes of rock cracking), it can be further explained that the existence of confining pressure limits the propagation of tensile stress and shear stress, leading to a lower degree of damage to cracks in the rock section and fewer branching cracks. Furthermore, the fact that the cracks in the rock section tend to distribute horizontally under confining pressure further indicates that the fragmentation trend of mechanical impact under confining pressure tends to follow the direction of maximum surrounding rock stress.

Extract the static water pressure curve of the rock element in the rock section under a single impact of a tool under a confining pressure of 4 MPa, and analyze the distribution of confining pressure in the rock section after mechanical impact rock breaking. As shown in Fig. 20, element H09767 is taken from the crack, element H10666 is taken from the crack edge, and element H11567 is taken from a distance from the crack edge. After the tool impacted the rock, element H09767 achieved complete damage, element H10666 suffered slight damage, and element H11567 did not suffer any damage. From the figure, before the tool impacts the rock, the confining pressure borne by the rock element is stable at around 4 MPa. Now when the tool impacts the rock, the rock element bears significant stress. After the tool comes out of contact with the rock (the single impact of the tool ends), the confining pressure

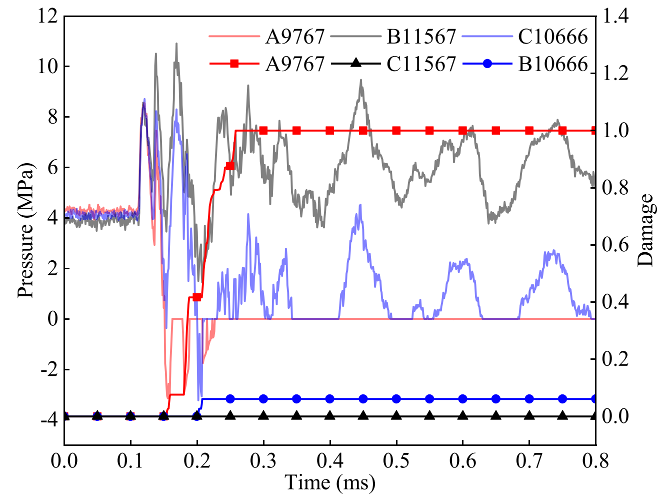

Fig. 20. Hydrostatic pressure and damage curve of rock elements at different positions.

borne by different rock elements at different positions shows a regular change. From the figure, after a single impact of the tool, the static water pressure of the rock element at the crack location returns to zero. The rock element along the crack edge (H10666) exhibits regular fluctuations around 0 MPa, while the overall amplitude of the static water pressure in the rock element further away from the crack edge is larger and fluctuates more violently. From this, it can be inferred that after the impact of the tool, the crack and undamaged rock elements closer to the edge of the crack have undergone unloading under confining pressure, but the undamaged rock elements are still subject to regular fluctuations under the influence of confining pressure factors. However, rock elements that have not suffered damage far from the crack still bear significant surrounding rock stress after being impacted by the tool. In addition, it can be seen from the graph that the peak hydrostatic pressure of the rock element is smaller as it approaches the crack location, and the rock element gradually begins to bear tensile stress.

Based on the analysis of the damage curve of the rock element, it can be concluded that although a confining pressure of 4 MPa increases the peak compressive stress borne by the rock element, the magnitude of the increase in compressive stress under confining pressure loading still cannot meet the rock fracture standard relative to the ultimate compressive strength of the rock. Through comprehensive analysis, it can be concluded that the unloading of confining pressure after mechanical impact on rocks mainly occurs at the crack and damage site, and the further away from the damage and crack, the greater the confining pressure.

4. Conclusions

In this paper, a numerical model of tool impact breaking in inhomogeneous rock is developed by random replacement to simulate the tool breaking process under unconfined and confined pressure conditions. Analyzed the process of mechanical impact rock fragmentation, rock damage mechanism, and the influence of confining pressure factors on rock damage distribution and crack propagation. The main conclusions obtained are as follows:

(1) Within the millisecond time scale, the rock-breaking process of the drop hammer method undergoes multiple cycles of tool impact and rebound impact. There is a phenomenon of cross-layer distribution and boundary layer ambiguity in the propagation of stress waves within heterogeneous rocks. The secondary impact of the tool will intensify the damage degree of existing

cracks and initiate more fine cracks, but it will not cause significant changes to the overall damage distribution of the rock.

(2) Tensile stress is the main cause of rock fracture, and the contribution of shear stress is smaller than that of tensile stress but greater than that of compressive stress. The distribution of tensile stress and the cumulative speed of damage along various directions of the rock determines the macroscopic fracture characteristics of the rock. The compression and shear stress are the main causes of rock failure at the mechanical impact point, and the cumulative damage of rock elements mainly occurs in the decreasing stage after the peak of stress. As the depth of rock damage increases, the compressive and shear stresses it bears rapidly decrease, while tensile stress gradually dominates mechanical rock breaking. The further away the rock element is from the impact site of the tool, the slower the cumulative damage speed, and it gradually shows a stepped cumulative trend.

(3) The presence of confining pressure mainly affects the distribution of tensile stress, thereby suppressing the propagation of internal cracks and damage in rocks. The unloading of confining pressure mainly occurs at the crack site, and the further away from the crack, the greater the confining pressure. During the process of tool impact rock breaking under confining pressure, the rock tends to fracture and fail along the direction of maximum surrounding rock stress.

CRediT authorship contribution statement

Huihe Zhao: Software, Writing – original draft. **Hongxiang Jiang:** Conceptualization, Methodology. **Zijian Wu:** Investigation. **Dongsheng Zhao:** Supervision. **Airong Wang:** Formal analysis.

Declaration of Competing Interest

The authors declare that they have no known competing financial interests or personal relationships that could have appeared to influence the work reported in this paper.

Acknowledgments

This work is financed by Jiangsu Provincial Post Graduate Research & Practice Innovation Program (KYCX25_2982), the Graduate Innovation Program of China University of Mining and Technology (2025WLKXJ094), the Natural Science Foundation of Jiangsu Province (BK20231497), and the National Key R&D Program of China (No. 2022YFC2905600).

Data availability statement

The computational data used in this study will be made available on request.

References

[1] X.H. Zhang, T. Tan, M. Li, et al., Research on rock breaking behaviors of different TBM hobs under grooving condition produced by water jet, Eng. Fail. Anal. 162 (2024) 108373.
[2] P. Wang, Z.W. Yue, A.K. Li, et al., Experimental and analytical study on key factors of rock breaking under a single indenter, Fatigue Fract. Eng. Mater. Struct. 46 (5) (2023) 1997–2016.
[3] Z.S. Ji, J.B. Jiang, H.Z. Shi, et al., Experimental studies on rock failure mechanisms under impact load by single polycrystalline diamond compact cutter, Pet. Sci. 20 (5) (2023) 3100–3109.
[4] R.X. Sun, J.L. Mo, M.Q. Zhang, et al., Cutting performance and contact behavior of partial-wear TBM disc cutters: A laboratory scale investigation, Eng. Fail. Anal. 137 (2022) 106253.
[5] S.F. Wang, L.C. Sun, Y. Tang, et al., Field application of non-blasting mechanized mining using high-frequency impact hammer in deep hard rock mine, Trans. Nonferrous Met. Soc. China 32 (9) (2022) 3051–3064.
[6] C. Li, Y.Q. Lu, Z. Chen, et al., Research status and prospect of rock breaking form in mechanized excavation of mining hard rock roadway, Coal Sci. Technol. 52 (S1) (2024) 259–268 (in Chinese).
[7] J. Liu, F.S. Ma, J. Guo, et al., Numerical simulation of failure behavior of brittle heterogeneous rock under uniaxial compression test, Materials 15 (19) (2022) 7035.
[8] Q. Qi, Y.S. Zhao, B.L. Li, et al., Spalling failure and fracturing of brittle sandstone containing rectangular cavity based on biaxial compression test and discrete element method, Eng. Fail. Anal. 158 (2024) 108035.
[9] W.J. Liu, Y.F. Wang, Z.W. Dan, et al., Micro-macro fracture mechanism of heterogeneous granite in percussive drilling, Pet. Sci. 20 (5) (2023) 3131–3142.
[10] D. Zhang, Y.X. Yang, H.T. Ren, et al., Experimental research on efficiency and vibration of polycrystalline diamond compact bit in heterogeneous rock, J. Pet. Sci. Eng. 220 (2023) 111175.
[11] S.R. Cao, Z.L. Ge, D. Zhang, et al., An experimental study of ultra-high pressure water jet-induced fracture mechanisms and pore size evolution in reservoir rocks, Int. J. Rock Mech. Min. Sci. 150 (2022) 104995.
[12] C. Zhang, S.L. Zhang, D.J. Zhao, Effect of amplitude and confining pressure on granite failure under ultrahigh frequency (UHF) impact based on radiation temperature, Geofluids 2022 (2022) 4817269.
[13] Y.L. Li, J.M. Peng, J.M. Li, et al., Theoretical and experimental study on single spherical button penetration into granite rock under dynamic impact loading, Rock Mech. Rock Eng. 55 (1) (2022) 213–233.
[14] Q.R. Wang, Q.H. Zhang, L.Y. Yang, et al., Study on stress evolution and crushing behavior of jointed rock mass under confining pressure and joint materials, Geofluids 2023 (2023) 6954611.
[15] Y.X. Wang, H. Lin, Y.L. Zhao, et al., Analysis of fracturing characteristics of unconfined rock plate under edge-on impact loading, Eur. J. Environ. Civ. Eng. 24 (14) (2020) 2453–2468.
[16] T.F. Guo, K.W. Liu, S.Z. Ma, et al., Dynamic fracture behavior and fracture toughness analysis of rock-concrete bi-material with interface crack at different impact angles, Constr. Build. Mater. 356 (2022) 129286.
[17] Y. Xi, H.Y. Wang, J. Li, et al., Transient process of mechanical response and energy conversion of rocks with different lithologies under impact loading, Geoenergy Sci. Eng. 228 (2023) 211978.
[18] J.F. Lu, T.B. Yin, W.X. Guo, et al., Dynamic response and constitutive model of damaged sandstone after triaxial impact, Eng. Fail. Anal. 163 (2024) 108450.
[19] Y. Wang, P.F. Tang, P. Li, et al., Effect of disturbed frequency on rock failure and energy characteristics exposed to triaxial fatigue and multistage unloading confining pressure (TF-MSUCP) conditions, Eng. Fail. Anal. 145 (2023) 106997.
[20] H. Hu, Q.Q. Zheng, X. Gao, et al., Fracture characteristics and geometric fractal of damaged sandstone under impact load, Shock Vib. 2020 (2020) 6617197.
[21] H.X. Jiang, Z.Y. Cai, H.H. Zhao, Numerical study of hard rock breakage under indenter impact by the hybrid FDEM, Eng. Fract. Mech. 233 (2020) 107068.
[22] X.C. Tian, T.J. Tao, C.J. Xie, Study of impact dynamic characteristics and damage morphology of layered rock mass, Geofluids 2022 (2022) 2835775.
[23] H.X. Jiang, H.H. Zhao, K.D. Gao, et al., Numerical investigation of hard rock breakage by high-pressure water jet assisted indenter impact using the coupled SPH/FEM method, Powder Technol. 376 (2020) 176–186.
[24] S.N. Li, Z.H. Huang, K. Huang, et al., Study on the evolution law and quantitative characterization of micro-crack propagation in the compressive failure process of rocks, Eng. Fail. Anal. 155 (2024) 107743.
[25] H.X. Jiang, H.H. Zhao, X.D. Zhang, et al., Numerical investigation of rock breaking by a dish-shape cutter with advance slotting, Eng. Fract. Mech. 289 (2023) 109393.
[26] P. Yuan, Q.H. Zhang, A.B. Li, Numerical analysis of cyclic impact damage evolution of rock materials under confining pressure, Appl. Sci. 13 (15) (2023) 8822.
[27] H. Zhang, H.J. Ni, B. Huang, et al., Research on discrete element modeling and numerical simulation of cutting rock behavior under impact load, Energy Sci. Eng. 10 (7) (2022) 2420–2436.
[28] W. Wang, G.H. Liu, J. Li, et al., Numerical investigation on rock-breaking mechanism and cutting temperature of compound percussive drilling with a single PDC cutter, Energy Sci. Eng. 9 (12) (2021) 2364–2379.
[29] J.F. Cao, D.Y. Zhou, C. Li, et al., Simulation analysis of igneous rock breaking law under cut-impact load, Chem. Technol. Fuels Oils 58 (5) (2022) 862–872.
[30] W. Gao, J. Li, C.Y. Wang, et al., Numerical investigation of impact fracture behaviors of rocks under confining pressure, Int. J. Fract. 245 (2024) 37–56.
[31] X.H. Zhu, Y.F. Wang, W.J. Liu, et al., A new method for evaluating the rock cutting and breaking performance of PDC cutters in heterogeneous granites, Nat. Gas Ind. 43 (4) (2023) 137–147 (in Chinese).
[32] H.S. Li, S.Y. Liu, J.G. Jia, et al., Numerical simulation of rock-breaking under the impact load of self-excited oscillating pulsed waterjet, Tunn. Undergr. Space Technol. 96 (2020) 103179.
[33] Z.L. Wang, H.C. Wang, J.G. Wang, et al., Finite element analyses of constitutive models performance in the simulation of blast-induced rock cracks, Comput. Geotech. 135 (2021) 104172.
[34] M. Kucewicz, P. Baranowski, J. Małachowski, Dolomite fracture modeling using the Johnson-Holmquist concrete material model: Parameter determination and validation, J. Rock Mech. Geotech. Eng. 13 (2) (2021) 335–350.
[35] C. Grunwald, B. Schaufelberger, A. Stolz, et al., A general concrete model in hydrocodes: Verification and validation of the Riedel–Hiermaier–Thoma model in LS-DYNA, Int. J. Prot. Struct. 8 (1) (2017) 58–85.
[36] T. Borrvall, W. Riedel, The RHT concrete model in LS-DYNA, Proceedings of the 8th European LS-DYNA Users Conference, Strasbourg, France, 2011.
[37] H.H. Zhao, H.X. Jiang, S. Warisawa, et al., Numerical study of abrasive water jet rotational slits in hard rock using a coupled SPH-FEM method, Powder Technol. 426 (2023) 118622.

[38] H.H. Zhao, H.X. Jiang, H.S. Li, et al., Numerical research on rock cutting by abrasive jet under confining pressure based on SPH-FEM method, Powder Technol. 433 (2024) 119196.
[39] L.X. Xie, W.B. Lu, Q.B. Zhang, et al., Analysis of damage mechanisms and optimization of cut blasting design under high in-situ stresses, Tunn. Undergr. Space Technol. 66 (2017) 19–33.
[40] H.C. Li, Y. Chen, D.S. Liu, et al., Sensitivity analysis determination and optimization of rock RHT parameters, J. Beijing Inst. Technol. 38 (8) (2018) 779–785 (in Chinese).
[41] X.T. Feng, Y.J. Wang, J.G. Yao, A neural network model for real-time roof pressure prediction in coal mines, Int. J. Rock Mech. Min. Sci. Geomech. Abstr. 33 (6) (1996) 647–653.
[42] M.F. Cai. Rock Mechanics and Engineering, first ed., Science Press, Beijing, 2002.

Hongxiang Jiang, Associate Professor and Doctoral Supervisor at China University of Mining and Technology. His main research interests focus on the high-pressure water jet technology, and rapid excavation technology for hard rock tunnels and deep earth engineering. He has led six projects, such as National Natural Science Foundation projects. His scientific research has been awarded 1 s Prize for Scientific and Technological Progress of the Ministry of Education.